Role of acoustic phonon transport in near- to asperity-contact heat transfer

Amun Jarzembski [1,2,*] Takuro Tokunaga,[1,*] Jacob Crossley [1] Jeonghoon Yun,[3] Cedric Shaskey [1]
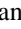Ryan A. Murdick,[4] Inkyu Park [3] Mathieu Francoeur [1,†] and Keunhan Park [1,‡]

[1]*Department of Mechanical Engineering, University of Utah, Salt Lake City, Utah 84112, USA*
[2]*Sandia National Laboratories, Albuquerque, New Mexico 87185, USA*
[3]*Department of Mechanical Engineering, Korea Advanced Institute of Science and Technology, Daejeon 34141, South Korea*
[4]*Renaissance Scientific, Boulder, Colorado 80301, USA*

Acoustic phonon transport is revealed as a potential radiation-to-conduction transition mechanism for single-digit nanometer vacuum gaps. To show this, we measure heat transfer from a feedback-controlled platinum nanoheater to a laterally oscillating silicon tip as the tip-nanoheater vacuum gap distance is precisely controlled from a single-digit nanometer down to bulk contact in a high-vacuum shear force microscope. The measured thermal conductance shows a gap dependence of $d^{-5.7\pm1.1}$ in the near-contact regime, which is in good agreement with acoustic phonon transport modeling based on the atomistic Green's function framework. The obtained experimental and theoretical results suggest that acoustic phonon transport across a nanoscale vacuum gap can be the dominant heat transfer mechanism in the near- and asperity-contact regimes and can potentially be controlled by an external force stimuli.

I. INTRODUCTION

Heat transfer between bodies separated by nanoscale vacuum gap distances has been extensively studied for potential applications in thermal management [1,2], energy conversion [3–6], and data storage [7]. For vacuum gap distances down to 10 nm, state-of-the-art experiments demonstrated that heat transport is mediated by near-field radiative heat transfer (NFRHT), which can greatly exceed Planck's blackbody limit [8–19]. By comparing measurements with theory based on fluctuational electrodynamics [20,21], the tunneling of evanescent electromagnetic waves has been unambiguously identified as the enhancement mechanism. In contrast, phonons become the dominant heat carrier when two objects are brought into contact [22]. This suggests that there should be a transition between electromagnetic wave-mediated NFRHT and phonon-mediated heat conduction in the near-contact regime.

Various theoretical studies have explored acoustic phonon transport across single-digit nanometer vacuum gaps as a plausible radiation-to-conduction transition mechanism [23–37]. These efforts have highlighted the roles of interatomic [23–33,35–37] and electrically driven force interactions [29,34,36] in mediating the so-called acoustic phonon tunneling phenomenon. Only one study experimentally explored acoustic phonon tunneling in the near-contact regime by implementing a scanning tunneling microscope with inelastic electron tunneling spectroscopy for thermal measure-

ment [38]. However, this work employed a simple photon emission model to support the presence of acoustic phonon tunneling and lacks rigorous comparison with measurements. Other studies have probed heat transfer for sub-10-nm vacuum gap distances [17,39–41], but have not linked heat transfer measurements across both the gap and contact regimes with a unified theoretical model to elucidate the existence of gap-mediated acoustic phonon transport.

This article presents experimental and theoretical results demonstrating that acoustic phonon transport can dominate heat transfer in the near- to asperity-contact regimes. To this end, we measure thermal transport from a feedback-controlled platinum (Pt) nanoheater to a flattened silicon (Si) tip in a high-vacuum shear force microscopy (HV-SFM) platform, which can precisely control the tip-nanoheater vacuum gap from single-digit nanometers to bulk contact. By selecting dissimilar materials (Pt and Si), NFRHT is effectively suppressed to make acoustic phonon transport the dominant heat transfer mechanism over the gap range considered [10]. Each of the experimental results are quantitatively compared with calculations based on the atomistic Green's function (AGF) method for acoustic phonon transport and fluctuational electrodynamics for NFRHT. The theoretical predictions indicate that acoustic phonon transport is driven by the Coulomb force interaction for near-contact vacuum gaps, which gives way to strong interatomic forces at the onset of contact. By analyzing the simultaneously measured tip-nanoheater thermal conductance and lateral force interaction, direct proportionality consistent with the AGF method is revealed and further emphasizes the role of acoustic phonon transport in the experiment. The results indicate acoustic phonon transport as a potential radiation-to-conduction transition mechanism, which can be used to develop active nanoscale thermal management systems.

*These authors contributed equally to this work.
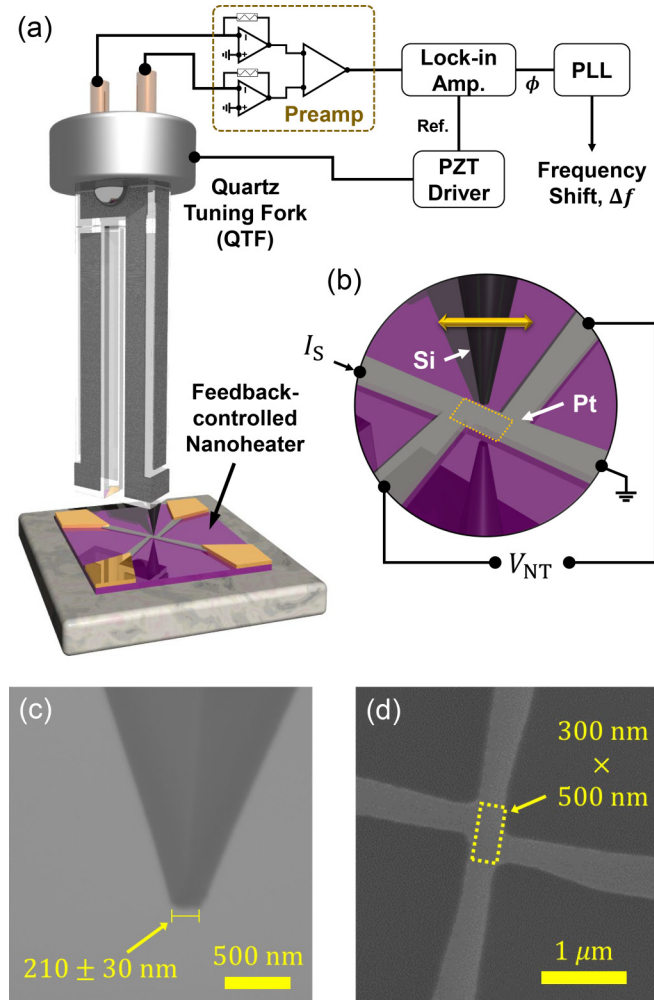†mfrancoeur@mech.utah.edu
‡kpark@mech.utah.edu

FIG. 1. (a) Experimental schematic based on a custom-built HV-SFM and feedback-controlled Pt nanoheaters. (b) Electrical schematic of the nanoheater four-point probe detection scheme with a laterally oscillating Si tip in close proximity. (c) SEM image of the Si tip, which exhibits a flat top geometry whose width is 210 ± 30 nm. (d) SEM image of the nanoheater device showing its maximum sensing area size of 300 nm $\times$ 500 nm.

II. HV-SFM/NANOHEATER EXPERIMENTS

A. Experimental setup

The HV-SFM, shown in Fig. 1(a), is a custom-built, high vacuum system (5×10^{-6} Torr in routine operations) that adopts a vertically aligned quartz tuning fork (QTF) probe having an Si tip at the free end of one prong for sensitive tip-sample lateral force measurement. The HV-SFM is equipped with a piezoelectric sample stage having an x,y,z-scanning range of 30 μm $\times$ 30 μm $\times$ 10 μm, respectively, and 16-pin electrical feedthroughs for electric connections during vacuum experiments. The vertical displacement of the sample stage is carefully calibrated to reveal a z-piezo sensitivity of 28.0 ± 2.8 nm/V with the position uncertainty of 1.8 Å [42], which is precise enough to control the vertical position of the tip with a subnanometer resolution.

When mechanically driven at the in-plane, antisymmetric resonant frequency ($f_0 = 32.768$ kHz), the QTF probe

exhibits a quality factor of $\sim$4000 in a high-vacuum environment. This high quality factor allows single-angstrom resolution for tip-sample gap control through monitoring the QTF's resonance frequency shift (i.e., $\Delta f = f - f_0$) [52]. According to the first-order QTF oscillator model, its resonance frequency shift enables quantification of the tip-sample conservative lateral force graidient ($\partial F_x / \partial z$) using $\partial F_x / \partial z \approx 2 k_{\text{eff}} \Delta f / f_0$ [53]. Here, the effective spring constant, k_{eff}, can be approximated as $k_{\text{eff}} \approx E w t^3 / (4 l^3)$, where $E = 7.87 \times 10^{10}$ N/m^2 is the Young's modulus of quartz [54]. Using the dimensions of the QTF prong ($l = 3.52$ mm; $w = 0.25$ mm; $t = 0.58$ mm), k_{eff} is estimated to be 22.0 kN/m. In addition, the vertically mounted QTF probe enables tip position stability above the sample surface with subnanometer gap control, which is not possible in the conventional cantilever-based method due to snap-in contact [17]. HV-SFM is also advantageous over the electron tunneling methodologies [38–41] as the QTF-mounted tip is not necessarily limited to electrically conductive materials. For the present study, an Si tip modified to a flat top, 210 ± 30 nm in width as shown in Fig. 1(c), is used to secure a sufficiently large heat transfer area as well as to implement a plane-plane configuration for theoretical modeling.

In order to minimize any effect of lateral tip motion onto the tip-nanoheater thermal transport measurement, the QTF oscillation amplitude is maintained within the subnanometer range. The lateral oscillation amplitude of a QTF probe was measured by optical fiber interferometry (OFI). As illustrated in Fig. S2(a) of the Supplemental Material [42], the optical fiber aperture is aligned to the sidewall of the tip-attached QTF prong to measure its lateral oscillation amplitude. The lateral oscillation amplitude of the tip (Δx_{tip}) is then estimated from the OFI measurement by using the QTF geometry. Both the electrical outputs from the QTF and OFI are simultaneously demodulated at the QTF resonant frequency to correlate Δx_{tip} with the QTF electrical signal (Δx_e). Figure S2(b) of the Supplemental Material [42] shows a linear correlation between Δx_{tip} and Δx_e, from which the QTF amplitude signal sensitivity is determined to be 7.32 ± 0.05 nm/V. The QTF electrical signal is set to $\sim$70 mV rms at its resonance frequency during experiments, which corresponds to a lateral tip motion of $\sim$0.5 nm rms. This lateral tip motion is on the order of the average lattice constant of the Si-Pt system [55,56] and is approximately three orders of magnitude smaller than the effective surface area subjected to thermal transport. Such a small lateral tip oscillation does not affect the thermal transport measurement.

The nanoheaters are batch fabricated using e-beam lithography for the nanopatterned Pt strip and photolithography for the micropatterned gold electrodes [44]. The Pt nanoheater has a sensing region of approximately 300 nm $\times$ 500 nm between the two inner electrodes, as marked by a yellow dashed box in Figs. 1(b) and 1(d), allowing a four-point probe electrical resistance measurement. When an electrical current (I_S) is supplied to the nanoheater for joule heating, the voltage drop (V_{NT}) across the inner electrodes is measured to monitor the electrical resistance of the nanoheater's sensing region (R_{NT}). For calibration, a nanoheater chip is placed on a heater stage equipped with a temperature controller (Cryo-Con, Model 22C) in the HV-SFM vacuum chamber. The sensing current

is set to $I_S = 100$ μA to minimize self-heating, while the entire nanoheater chip is bulk heated in a high vacuum condition [57]. Figure S3 in the Supplemental Material shows the calibration results of two nanoheaters (nanoheater no. 1 for the near-contact measurements and nanoheater no. 2 for the bulk-contact measurements) [42], demonstrating that R_{NT} is linearly proportional to the substrate temperature T_S (or the sensing area temperature T_{NT}). The resultant temperature coefficient of resistance (TCR) is 1.2×10^{-3} K^{-1} for nanoheater no. 1 and 9.6×10^{-4} K^{-1} for nanoheater no. 2, respectively. Moreover, the sensing region of the nanoheater can be joule heated up to ∼500 K by increasing power dissipation (i.e., $P_{NT} = I_S \times V_{NT}$). From the obtained linear correlation between T_{NT} and P_{NT}, the effective thermal resistance of the sensing region ($R_{th,NT} = \Delta T_{NT}/\Delta P_{NT}$) is determined to be 0.533 ± 0.008 K/μW for nanoheater no. 1 and 0.485 ± 0.004 K/μW for nanoheater no. 2. Although the nanoheater TCRs are obtained in the temperature range less than 350 K due to the limit of the heating stage, the linearity measured between T_{NT} and P_{NT} signifies that the obtained TCRs are valid for higher temperatures.

Since the tip side has no sensing component, the nanoheater should measure both the heat transfer rate to the tip (Q_{tip}) and the sensing region temperature (T_{NT}) as the tip approaches the nanoheater. To this end, the electrical current is feedback controlled to compensate tip-induced thermal transport, while T_{NT} is maintained at a set-point value [57]. For the optimal response time and noise suppression of the nanoheater, an eighth-order low pass filter with 10 Hz cutoff frequency is implemented while the feedback integration gain is set to 20 V/Ωs. Figure S4 in the Supplemental Material demonstrates the feedback control result of nanoheater no. 1 [42]. When the temperature set point is dropped from 481.93 K (or $R_{NT} = 7.12\Omega$) to 479.17 K ($R_{NT} = 7.10\Omega$) and returned back to 481.93 K, T_{NT} responds to the stepwise set-point changes within a settling time of ∼0.5 s and an overshoot temperature of ∼0.5 K by changing P_{NT} by ∼3 μW. The noise-equivalent temperature (NET) and noise-equivalent power (NEP) of the feedback-controlled nanoheater sensing region can be determined by conducting a time-based statistical analysis of the T_{NT} and P_{NT} traces [58]. When nanoheater no. 1 is feedback controlled at the set point of 481.93 K and the sampling rate of 500 Hz, its NET and NEP are measured to be 32 mK and 36 nW, respectively. We note that the low pass filter sufficiently eliminates the power noise at 60 Hz, yielding a three times improvement in the NEP when compared with the previous result [57]. The measured NEP value is in good agreement with the NEP estimated from $R_{th,NT}$ (i.e., NEP $=$ NET/$R_{th,NT} \approx 60$ nW) [59]. The evaluated NEP confirms that the feedback-controlled nanoheater can measure the tip-induced heat transfer rate in the near-contact regime, which can be as small as ∼100 nW for the present study.

B. Experimental procedures

To consistently describe the thermal and force interactions around contact, we define the tip-nanoheater gap (d) as the distance between the mean lines of the tip and nanoheater surface profiles. To avoid any undesired inaccuracy due to surface contamination, both the tip and nanoheater surfaces
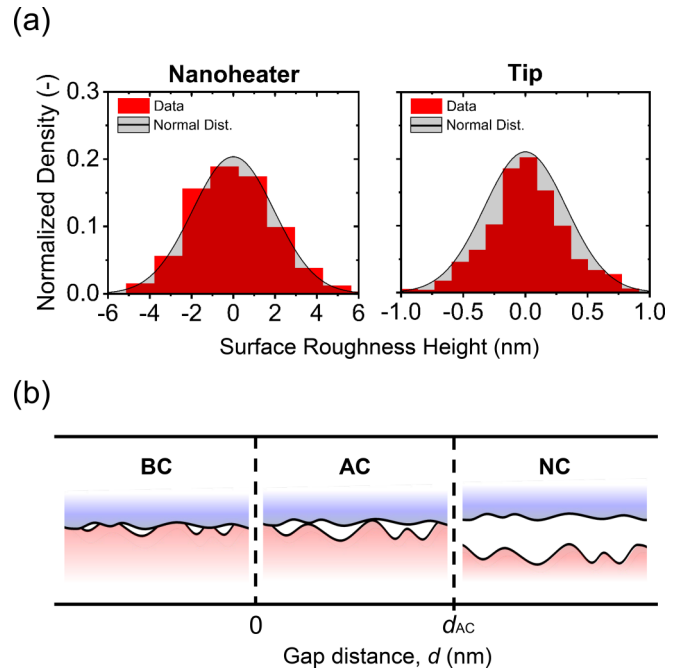

FIG. 2. (a) Measured surface roughness distributions of the nanoheater and tip, which have nominal peak heights of 5.0 ± 0.1 nm and 0.86 ± 0.01 nm, respectively, as measured within a 98% confidence interval. (b) Illustration of the gap distance (d) defined between the mean lines of the flattened Si tip and Pt nanoheater surface profiles showing three regimes defined based on the gap distance, i.e., bulk contact (BC), asperity contact (AC), and near contact (NC).

undergo cleaning procedures outlined in Appendix A. The surface profiles of both the Pt nanoheater sensing region and flattened Si tip are then measured by atomic force microscopy as described in Appendix B. As shown in Fig. 2(a), the measured surface profiles for both surfaces follow Gaussian distributions, from which the surface roughness is determined to be $R_{p,NT} = 5.0 \pm 0.1$ nm for the nanoheater sensing area and $R_{p,tip} = 0.86 \pm 0.01$ nm for the Si tip within a 98% confidence interval. As illustrated in Fig. 2(b), the bulk-contact (BC) regime is thus defined as $d \leqslant 0$, where the majority of surface asperities are in solid contact. The near-contact (NC) regime is where d is larger than the surface peak heights (i.e., $d > d_{AC}$, where $d_{AC} \approx R_{p,tip} + R_{p,NT}$) to ensure no contact between surface asperities. The asperity-contact (AC) regime resides between the BC and NC regimes.

The benefit of combining the feedback-controlled nanoheater and HV-SFM platform is the simultaneous measurement of tip-induced thermal transport and conservative tip-nanoheater lateral force interaction. Figure 3 shows the Δf and T_{NT} traces, respectively, as the sensing region of the feedback-controlled nanoheter approaches the Si tip. The approaching speed of the sample stage is 0.75 nm/s to provide sufficient time to stabilize T_{NT} at the set point of 467.13 K within $\pm$50 mK accuracy. While Δf monotonically increases as the nanoheater approaches the tip, its z derivative shown in the inset clearly shows a drastic drop when the tip makes bulk contact with the nanoheater surface. The onset of bulk contact can also be confirmed by the T_{NT} trace,
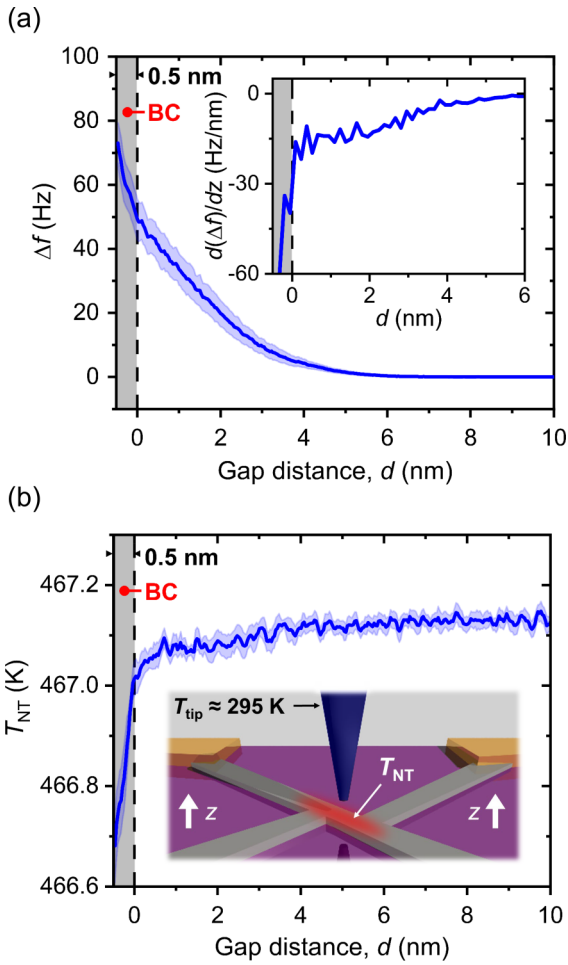
(a)

(b)

FIG. 3. (a) Measured Δf of the QTF, illustrating the monotonic increase of tip-sample lateral forces with decreasing d. At BC, this variation becomes more rapid as denoted by its z-derivative drop at 0 nm (inset). (b) Feedback-controlled T_{NT} trace as the nanoheater approaches the tip at room temperature (i.e., $T_{tip} \approx 295$ K). In this figure, the solid lines show the average of 13 measurements whose 95% confidence interval is denoted by the blue shaded region.

which drops at the mechanically determined BC point. The nanoheater feedback controller, which is optimized to provide the best signal-to-noise ratio in T_{NT} and P_{NT} measurements, is not fast enough to fully respond to the abrupt increase of conduction heat transfer through the bulk-contacted Si-Pt interfaces. The slow feedback control is also responsible for the slight drift of T_{NT} by ~0.1 K from the set point when the tip is in the AC regime near the BC point. Nevertheless, this result suggests that the onset of BC can be concurrently determined from mechanical and thermal signals and be used as a reference point for the tip-nanoheater gap distance (i.e., $d = 0$).

The heat transfer rate from the nanoheater sensing region to the tip (Q_{tip}) can be measured by monitoring P_{NT} that changes to maintain T_{NT} at a set point while the tip approaches the nanoheater sensing region. However, it should be noted that T_{NT} is the averaged temperature of the nanoheater sensing region. Although T_{NT} is maintained constant under feedback control, tip-induced local cooling perturbs a temper-

ature distribution of the nanoheater to cause heat conduction from the joule-heated electrical leads to the sensing region (Q_{lead}). The tip-based heat transfer rate is thus determined by $Q_{tip} = \Delta P_{NT} + Q_{lead}$. Based on the effective thermal network analysis, Q_{lead} can be modeled as $Q_{lead} = 2\mathcal{L}_0 T_{NT} L_{NT} (T_{NT} - T_\infty) \Delta P_H / (L_{lead} R_{NT} P_{H,0})$, where $\mathcal{L}_0 = 2.44 \times 10^{-8}$ WΩ/K^2 is the Lorentz number, L_{NT} is the length of the sensing region, L_{lead} is the effective length of the lead from the inner electrode to the lead hotspot, and ΔP_H is the difference of power dissipation in the lead with ($P_{H,1}$) and without ($P_{H,0}$) tip-induced cooling. The derivation of Q_{lead} and details of notation are provided in Sec. I D of the Supplemental Material [42]. When T_{NT} is set to 467.13 K, Q_{lead} is estimated to be ~4.2% of the measured ΔP_{NT}. The experimental thermal conductance is then defined as $G_{expt} = Q_{tip}/\Delta T$, where $\Delta T = T_{NT} - T_{tip}$ is the temperature difference between the nanoheater sensing region and the tip apex. Since T_{tip} is not directly measurable, it is assumed to be the same as the tip base temperature at $T_{tip} = 295 \pm 0.05$ K. Section I E of the Supplemental Material supports this assumption by numerically calculating the thermal conductance of the tip, which is two orders of magnitude greater than the BC thermal conductance [42].

C. Measurement of G_{expt}

In Fig. 4(a), the experimental thermal conductance G_{expt} shows a monotonically increasing trend as the gap distance d decreases, approaching the adjusted BC thermal conductance (G_{BC}^*) of 58.9 ± 3.7 nW/K. It should be noted that G_{BC}^* was separately measured using a cantilever probe and adjusted by considering the difference in tip apex geometry: see Appendix C for more details. When G_{expt} is replotted on a log-log scale as shown in the inset of Fig. 4(a), the G_{expt} curve displays different gap dependencies between the NC regime and the AC regime. In the NC regime, G_{expt} increases by an order of magnitude from the nanoheater noise threshold (i.e., 0.4 nW/K) following a $d^{-5.7}$ power law. In order to confirm the reproducibility of the observed NC gap dependence (d^n), we repeated the measurement 80 times using three different tip-nanoheater sets and extracted n values. Each data fits well with the d^n function in the NC regime as quantified by an average R^2 value of 0.87. Figure 4(b) shows the histogram of n values, which is well represented by a Gaussian distribution to yield $n = -5.7 \pm 1.1$. On the other hand, the AC regime exhibits a smaller gap dependence than $d^{-5.7}$ due to the increasing contribution of conduction heat transfer through asperity contacts. In the AC regime, G_{expt} increases by another order of magnitude approaching G_{BC}^* at $d = 0$.

III. THEORETICAL MODELING

The experimental thermal conductance G_{expt} conveys a combination of noncontact and contact heat transfer mechanisms that are complicated to model. The gap dependence of G_{expt} in the NC regime (i.e., $d^{-5.7 \pm 1.1}$) is much steeper than what has been predicted with the existing NFRHT models for the tip-plane configuration [8,17,60,61], suggesting that NFRHT may not be the dominant heat transfer mechanism in the NC regime. To elucidate the physics underlying the measured thermal conductance, the theoretical thermal
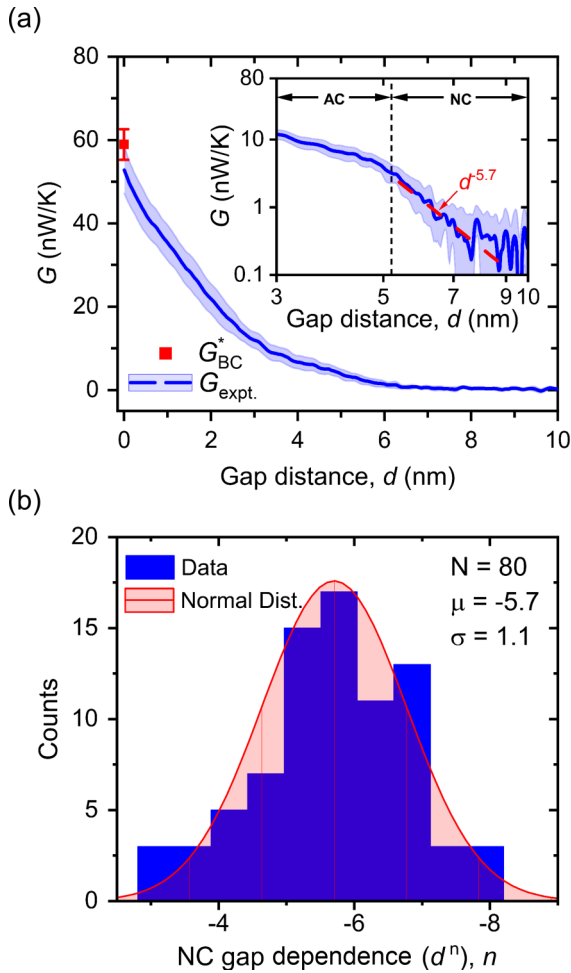
FIG. 4. (a) Measured thermal conductance (G_{expt}) as d is reduced to BC. Measured thermal conductance replotted on a log-log scale in the inset to show the gap dependence in the NC regime. In this figure, the solid lines show the average of 13 measurements whose 95% confidence interval is denoted by the blue shaded region. (b) The distribution of the NC gap dependence (d^n) from 80 measurements, demonstrating its repeatability at $n = -5.7 \pm 1.1$.

FIG. 5. (a) Theoretical heat transfer coefficients for varying interatomic distance (δ) computed by fluctuational electrodynamics for NFRHT and the AGF method, where individual AGF contributions are given by the Lennard-Jones (L-J) and Coulomb forces. The possible inaccuracy of NFRHT predictions for $\delta < 2$ nm is emphasized via a dotted line. (b) Phonon transmission function through the vacuum space calculated with the AGF method.

conductance, G_{theory}, is calculated by considering acoustic phonon transport and NFRHT between tip and nanoheater surfaces that are regenerated based on the measured surface roughness distribution. Since commercial Si microcantilevers are typically n doped, we consider that the Si tip is n doped with phosphorus at 1×10^{18} cm^{-3} based on the electrical resistance range provided by the manufacturer. The heat transfer coefficient due to electron tunneling has also been calculated using the framework described in Ref. [36] and its contribution has been found to be orders of magnitude smaller than the other heat transfer mechanisms. Throughout the following discussion, the subscripts L and R refer to the left and right regions that are respectively made of Pt and Si. The temperatures of the left and right regions are fixed at $T_L = 470$ K and $T_R = 300$ K.

A. Heat transfer coefficient contributions

Heat transfer due to acoustic phonon transport is calculated via the AGF method [62] applied to a one-dimensional (1D)
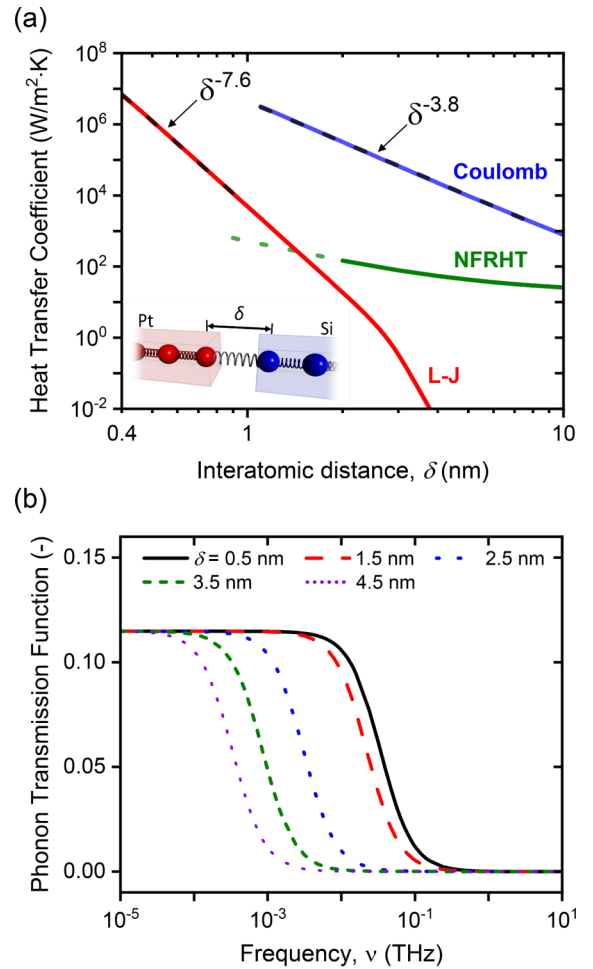
Si-Pt atomic chain that has an interatomic vacuum gap distance δ: see the inset of Fig. 5(a) for the schematic of the 1D atomic chain. The heat flux due to acoustic phonon transport across the interatomic vacuum distance δ for the 1D atomic chain is given by [62]

$$q_{ph} = \frac{1}{A_{Si-Pt}} \int_0^\infty d\omega \frac{\hbar\omega}{2\pi} \mathcal{T}_{ph}(\omega)[N(\omega, T_L) - N(\omega, T_R)].$$

(1)

Here, $N = 1/[\exp(\hbar\omega/k_b T) - 1]$ is the Bose-Einstein distribution function, where $\hbar$ is the reduced Planck constant and k_b is the Boltzmann constant. The effective heat transfer area, A_{Si-Pt}, is the projected atomic area calculated using an average atomic radius, i.e., $A_{Si-Pt} = \pi(r_{Pt} + r_{Si})^2/4$, where $r_{Pt} = 1.77 \times 10^{-10}$ m and $r_{Si} = 1.11 \times 10^{-10}$ m are the atomic radius of Pt and Si, respectively [63]. The phonon transmission function, $\mathcal{T}_{ph}$, is derived from the AGF method by modeling Pt and Si as semi-infinite leads separated by a device region. The device region contains atoms of Pt and Si separated by the

vacuum gap. The phonon transmission function is written as

$$\mathcal{T}_{ph}(\omega) = \text{Trace}[\Gamma_L G_d \Gamma_R G_d^\dagger], \qquad (2)$$

where the superscript † denotes conjugate transpose. The escape rate of phonons from the device region to the semi-infinite leads, $\Gamma_{L(R)}$, is defined as

$$\Gamma_{L(R)} = i[\Sigma_{L(R)} - \Sigma_{L(R)}^\dagger], \qquad (3)$$

where $\Sigma_{L(R)}$ is the self-energy matrix that can be written as $\Sigma_{L(R)} = \tau_{L(R)} g_{L(R)} \tau_{L(R)}^\dagger$. Here, $\tau_{L(R)}$ is the coupling matrix connecting the left (L) or right (R) semi-infinite lead with the device region. The coupling matrix is computed via the force constant between the atoms bounding the semi-infinite leads and the device region, and the atomic masses. The atomic masses of Pt and Si are 3.239×10^{-25} kg and 4.664×10^{-26} kg, respectively [64]. The term $g_{L,R}$ is the uncoupled Green's function (also called surface Green's function) derived from the harmonic matrix of the left (L) or right (R) semi-infinite lead. The uncoupled Green's function is computed using the decimation technique described in Ref. [62]. In Eq. (2), the device Green's function (G_d) is given by

$$G_d = [\omega^2 I - H_d - \Sigma_L - \Sigma_R]^{-1}, \qquad (4)$$

where I is the identity matrix and H_d is the harmonic matrix of the device region.

Heat transfer due to acoustic phonon transport is mediated by short-range and long-range forces in the vacuum region. The overlapping electron cloud repulsive force and van der Waals (vdW) force interactions, modeled by the Lennard-Jones (L-J) potential with empirical parameters for Pt and Si [65], and the Coulomb force due to surface charges on the nanoheater sensing region, are considered as interatomic forces that virtually connect the Pt and Si atomic chains. Details regarding calculation of force constants acting in the vacuum space are provided in Appendix D. The force constants are then included in the harmonic matrix H_d following the procedure described in Appendix E. The heat transfer coefficient is finally obtained by dividing the heat flux by the temperature difference, i.e., $h_{ph} = q_{ph}/\Delta T$. Five atoms of Pt and five atoms of Si in the device region are sufficient to obtain stable and converged results. Note that although the 1D AGF calculation does not capture the angle dependence of phonon propagation and force interactions with neighboring atoms, a previous work [25] demonstrated that phonon transport becomes quasi 1D in the NC regime. This has also been verified by comparing 1D AGF results against three-dimensional lattice dynamics results [26]: more discussion on the verification of the 1D AGF method for calculating interfacial and near-contact acoustic phonon transport is provided in Sec. II of the Supplemental Material [42].

The heat transfer coefficient due to NFRHT is calculated using fluctuational electrodynamics [21], where Pt and Si are modeled as two semi-infinite planes [20,36]. The dielectric functions are taken from Ref. [66] for Pt and Refs. [67,68] for n-doped Si. The radiative heat transfer coefficient is calculated down to an interatomic vacuum distance δ of 1 nm. However, since fluctuational electrodynamics is a theory based on the macroscopic Maxwell equations that is unlikely to be valid

for such a small distance, the NFRHT results below $\delta = 2$ nm are plotted with a dotted curve.

Figure 5(a) shows the individual contribution of the L-J and Coulomb forces to the AGF-calculated acoustic phonon heat transfer coefficient for the 1D Si-Pt atomic chain. While the L-J force model drives heat transfer for $\delta < 1.1$ nm, the Coulomb force becomes a dominant contributor for larger δ values (i.e., 1.1 nm $< \delta <$ 10 nm). This significant contribution of the Coulomb force arises from surface charges induced by the local voltage bias at the center of the nanoheater sensing region (0.8 V from the ground) when it is joule heated at $T_{NT} = 467.13$ K. Here, we assume that the Coulomb force vanishes for $\delta < 1.1$ nm due to surface charge neutralization between the nanoheater and tip: see also Appendix D. As a result, acoustic phonon heat transfer between Pt and Si surfaces can exceed NFRHT for interatomic distances up to $\delta \sim 10$ nm. The potential inaccuracy of the NFRHT calculations has no impact on the theoretical thermal conductance since heat transfer is largely dominated by acoustic phonon transport for $\delta < 2$ nm. The calculated heat transfer coefficients follow power laws of $\delta^{-7.6}$ for the L-J force and $\delta^{-3.8}$ for the Coulomb force, respectively, illustrating that the experimental value of $d^{-5.7}$ could be indicative of acoustic phonon transport. Figure 5(b) shows the phonon transmission function calculated by the AGF method, where the dominant frequency range of phonon transmission is below $\sim$1.0 THz at $\delta = 0.5$ nm. The phonon dispersion curves and density of states for bulk Pt and Si [56,69] confirm that acoustic phonons are the dominant heat carriers across the vacuum distance in the NC regime.

B. Comparison between G_{expt} and G_{theory}

For fair comparison with G_{expt}, the theoretical thermal conductance (G_{theory}) is calculated by implementing surface features of the flattened Si tip and the Pt nanoheater sensing region in the AGF calculation. To this end, both surfaces are randomly regenerated from the measured surface roughness distributions shown in Fig. 2(a) and discretized into N flat pixels having different gap distances. Once the local heat transfer coefficient h_i is calculated by applying the 1D AGF for each pixel, the thermal conductance is approximated as $G_{theory}(d) = \sum_{i=1}^{N} h_i(\delta_i) A_i$, where A_i is the pixel area and δ_i is the local interatomic distance for each pixel. The minimum value of δ_i (i.e., contact) is set to 4.68 Å, which is the average value of the lattice constants for Pt (3.92 Å) [55] and Si (5.43 Å) [56]. The effective heat transfer area, limited by the Si tip surface, is determined based on the SEM image shown in Fig. 1(c). We approximate the Si tip surface as a square whose diagonal length is 240 nm, yielding $A_{tip} = (240 \times 10^{-9}/\sqrt{2})^2 = 2.88 \times 10^{-14}$ m^2. A_{tip} is discretized into N subsurfaces of equal size (i.e., $A_i = A_{tip}/N$). A convergence analysis revealed that $N = 1024$ is sufficient to obtain stable results. In order to develop statistically relevant predictions, G_{theory} is calculated from 30 regenerated surfaces, which results in 30 sets of $G_{theory}(d)$.

Figure 6(a) compares G_{theory} and G_{expt} on linear-linear and log-log scales (inset), demonstrating strong agreement between them for both NC and AC regimes. The bold dashed lines (green color) correspond to the theoretical thermal
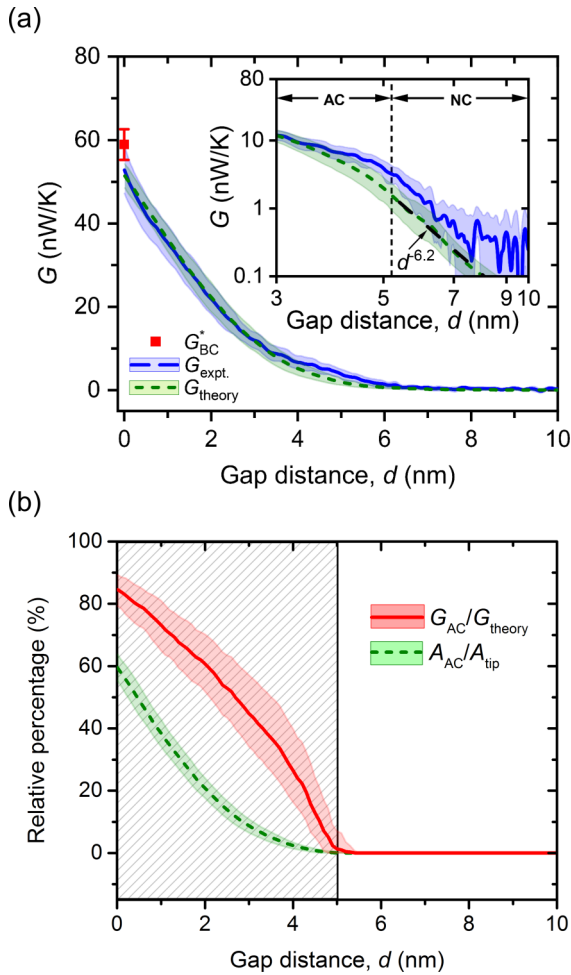
(a)

(b)

FIG. 6. (a) Theoretical and experimental thermal conductances on linear-linear and (inset) log-log scales. (b) Calculated AC thermal conductance ratio (G_{AC}/G_{theory}, where $G_{theory} = G_{NC} + G_{AC}$) and asperity contact area ratio (A_{AC}/A_{tip}), showing the transition between the NC and AC regimes.

ratio (A_{AC}/A_{tip}, where A_{AC} is the asperity-contact area and A_{tip} is the total tip area). While both G_{AC}/G_{theory} and A_{AC}/A_{tip} are 0% in the NC regime signifying noncontact heat transfer, they start to increase at $d_{AC} \approx 5.2$ nm due to the onset of asperity contacts. It should be noted that the vertical dashed line drawn in the inset of Fig. 6(a) denotes d_{AC}, which is in agreement with the aforementioned definition of the NC and AC regimes (i.e., $d_{AC} \approx R_{p,tip} + R_{p,NT}$) based on the surface roughness. At $d = 0$, G_{AC} reaches ~80% of G_{theory}, while A_{AC} becomes ~60% of A_{tip}, theoretically supporting the smooth transition from near-contact to bulk-contact heat transfer by means of acoustic phonon transport.

Since acoustic phonon transport across a vacuum gap is mediated by interatomic force interactions between Pt and Si atoms, the impact of each force contributing to G_{theory} is

(a)

(b)
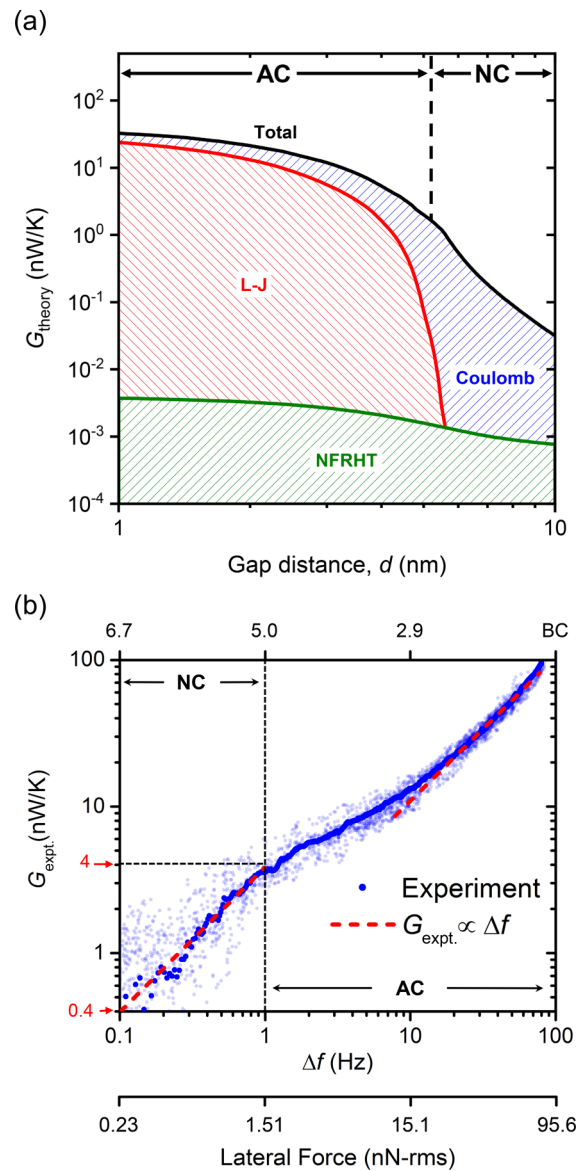
FIG. 7. (a) AGF force model contributions to G_{theory} are compared with NFRHT, which is provided as a reference. (b) G_{expt} correlation with the simultaneously acquired Δf, where Δf is related to the tip-sample lateral force.

conductance averaged over 30 regenerated surfaces, while the shaded regions (green color) are produced by calculating $G_{theory}^{average} \pm 2\sigma$, where σ is the standard deviation for the upper and lower bounds of the surface charge density: see Appendix D. The gap dependence of G_{theory} in the NC regime is -6.2 ± 0.4, which is consistent with the measured gap dependence of $d^{-5.7 \pm 1.1}$ within the uncertainty. In addition, the theoretical thermal conductance at $d = 0$ (54.2 nW/K) is in good agreement with the bulk thermal conductance values measured with the QTF probe (52.8 nW/K) and the cantilever probe (58.9 nW/K). These well-agreed experimental and theoretical results strongly suggest that acoustic phonon transport plays a significant role in heat transfer between Si and Pt for both the NC and AC regimes, possibly being the mechanism bridging radiation and conduction heat transfer. Moreover, the AGF method can separate the contributions of phonon transport through the vacuum gap (G_{NC}) and asperity contacts (G_{AC}) towards the total thermal conductance (i.e., $G_{theory} = G_{NC} + G_{AC}$). Figure 6(b) shows the asperity-contact thermal conductance ratio (G_{AC}/G_{theory}) and the asperity-contact area

calculated with the AGF method and shown in Fig. 7(a). Here, NFRHT is also included for comparison. In the AC regime, the short-range force interactions, such as the repulsive force due to overlapping electron clouds and the vdW force, dominate thermal transport. However, the Coulomb force becomes a dominant contributor in the NC regime, allowing acoustic phonon transport to exceed NFRHT by up to three orders of magnitude. When considering the origin of the Coulomb force, our calculation suggests the possibility of manipulating heat transfer in the NC regime with external force stimuli [29]. Figure 7(b) further demonstrates the strong correlation between tip-surface heat transfer and force interactions by comparing G_{expt} to the simultaneously acquired Δf of the QTF. As the contact regime transitions from AC to BC, G_{expt} becomes linearly proportional to Δf as indicated by the red dashed line in the top right corner of Fig. 7(b). Since the lateral force gradient exerted on the tip can be first-order approximated as $\partial F_x/\partial z \approx 2 k_{\mathrm{eff}} \Delta f / f_0$ [53], the lateral force at different gaps can be calculated by integrating the equation over the interval $d \leqslant z \leqslant \infty$. The calculated lateral force is denoted in Fig. 7(b) along with Δf. Since the lateral force can be related with the normal force by the nanoscale friction law [70], the observed linear proportionality in the AC-to-BC transition indicates a strong correlation between the normal contact force and the interfacial thermal conductance. Interestingly, a similar linear proportionality between G_{expt} and Δf is observed in the NC regime as indicated by the red dashed line in the bottom left corner, implying that Pt and Si atoms are still connected by interatomic forces to allow noncontact acoustic phonon transport. We also experimentally demonstrate that the tip-sample lateral force increases with the increasing electrical current supplied to the nanoheater in the NC regime (Sec. III of the Supplemental Material [42]), which we believe should increase the thermal conductance. However, the manipulation of the near-contact thermal conductance by external force stimuli was not measured due to limitations in the current nanoheater design, which remains for future research.

IV. CONCLUSIONS

We have conducted experiments of thermal transport between a flattened Si tip and feedback-controlled Pt nanoheater in a high-vacuum shear force microscope (HV-SFM) as the tip is positioned in the near-contact (NC), asperity-contact (AC), and bulk-contact (BC) regimes with the nanoheater surface. The obtained experimental results clearly show that heat transfer in the NC regime is much greater than NFRHT with a stronger gap dependence. Comparison of the experimental data with heat transfer calculations based on the atomistic Green's function method and fluctuational electrodynamics frameworks provides evidence that acoustic phonons can be transported not only through asperity contacts but also across nanoscale vacuum spaces due to force interactions between terminating atoms separated by vacuum. This finding sheds light on the possibility of engineering interfacial thermal transport using external force stimuli, which can impact the development of next-generation thermal management technologies.

APPENDIX A: SURFACE CLEANING PROCEDURES

To ensure that the interacting surfaces are free from contamination prior to experiments, a routine surface inspection and cleaning protocol was established for the QTF probes and nanoheaters. First, several QTF probes and nanoheaters are inspected using scanning electron microscopy (SEM) to select the ones with no major debris around the sensing areas: see Figs. 1(c) and 1(d). After initial sonication cleaning with acetone, they are placed in a deep ultraviolet (UV) ozone cleaner (Novascan, PSD-UV4) to remove organic contamination using UV light at 185 and 254 nm in wavelength [72]. The UV-ozone cleaner is set to generate ozone for 2 h. After UV treatment, the QTF probe and the nanoheater are promptly mounted to the HV-SFM, which is evacuated to high vacuum to minimize undesired exposure to the ambient before experiments [41]. Moreover, all experiments were carried out at high temperature (i.e., 467 K), which inherently removes weakly bonded contaminants from the surface.

APPENDIX B: SURFACE ROUGHNESS CHARACTERIZATION

In order to secure a sufficient heat transfer area, the Si tip was flattened by long-line scanning on the nanoheater substrate (i.e., a 500-nm-thick silicon nitride film on top of a silicon substrate) at a contact force of $\sim$10 nN. Once the flattened tip was attached to the QTF, the tip was long-line scanned on the nanoheater substrate again in asperity contact mode for the fine adjustment of surface parallelism. Since the surface profiles play a pivotal role in determining different contact regimes, we measured the surface roughness distributions of both the nanoheater sensing region and flattened Si tip. The nanoheater surface profile was obtained by soft-contact AFM imaging, as marked by a yellow rectangle in Fig. 1(d). A small contact force ($\lesssim$ 3 nN) during the AFM imaging results in a contact diameter of $\sim$8 nm as estimated by the Hertzian model [73]. A surface roughness histogram of the nanoheater sensing region from the obtained AFM image

shows a Gaussian distribution centered at 0 nm with a standard deviation of $\sigma = 1.96$ nm; see Fig. 2(a). The equivalent surface peak height is $R_{p,\mathrm{NT}} = 5.0 \pm 0.1$ nm within a 98% confidence interval. The surface profile of a flattened Si tip was determined by tapping-mode topographic imaging of a calibration sample consisting of sharp pyramids (K-TEK Nanotechnology, TGT1), whose apex radii are nominally 17 nm. Since the sample pyramids are much sharper than the flattened Si tip, the resulting convoluted tip-sample AFM image provides the surface roughness profile of the flattened tip. A surface roughness histogram of the flattened tip area from the convoluted AFM image displays a Gaussian distribution centered at 0 nm with a standard deviation of $\sigma = 0.33$ nm, as shown in Fig. 2(a). The equivalent surface peak height is $R_{p,\mathrm{tip}} = 0.86 \pm 0.01$ nm within a 98% confidence interval.

APPENDIX C: MEASUREMENT OF BULK-CONTACT THERMAL CONDUCTANCE

To fully understand the transition from NC to BC thermal transport, the tip should approach the nanoheater sensing region to form BC while avoiding damage to the tip and nanoheater. However, the high vertical rigidity of the QTF can easily damage both the tip and nanoheater when the tip is further pushed once BC is made. To address this challenge, we conducted BC measurements separately by using a cantilever in high vacuum [see Fig. S7(a) in the Supplemental Material [42]]. It should be noted that our HV-SFM also has a regular AFM head for cantilever-based operations. The cantilever used in the BC experiment is the same model (Bruker, FMV-A) as that mounted to the QTFs for the NC and AC measurements. The cantilever deflection is detected by an optical fiber interferometer aligned with the cantilever's backside [43]. Nanoheater no. 2 was used for the BC measurement [topography shown in Fig. S7(b)], whose sensing area is 330 nm × 375 nm. After AFM topographic imaging with soft-contact mode ($F_z \lesssim 3$ nN), the force spectroscopy measurement was conducted by approaching the tip to the nanoheater sensing region until they make hard contact ($F_z \gtrsim 15$ nN). An SEM image of the Si tip after the force spectroscopy is shown in Fig. S7(c). We believe that bulk contact is made at the flattest portion of the tip apex to form the contact diameter of 215 ± 25 nm.

For both the cantilever- and QTF-based experiments, the nanoheater current (I_S) is feedback controlled, while the voltage drop across the sensing region (V_{NT}) is measured for real-time monitoring of T_{NT}. The only difference in the cantilever-based measurements is that after snap in contact is made, the cantilever is further pushed to achieve BC between the tip and nanoheater. Figure 8 presents the cantilever deflection and T_{NT} signals as a function of the tip position. At a distance of 5 nm, the cantilever snaps into contact as denoted by the sudden drop of the cantilever deflection and T_{NT}. As the tip is continuously pushed toward the nanoheater, the cantilever returns to its neutral position, which is referred to as the zero z-displacement position [17]. In the negative displacement regime, the sample pushes the cantilever to bend backwards such that bulk contact is made with a sufficient contact force. Meanwhile, the feedback controller settles T_{NT} to the set point by increasing the heating power. Figure 8 also
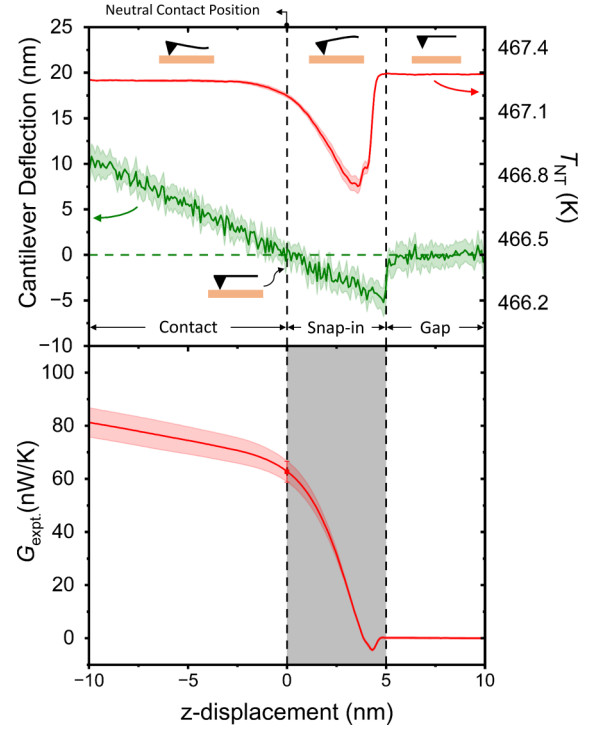

FIG. 8. Measurement of the bulk-contact thermal conductance (G_{BC}) for the Si-Pt system. Cantilever deflection and feedback-controlled temperature signal (top) and the measured value of G_{expt} (bottom) are plotted as a function of the z displacement. Here, G_{BC} for the Si-Pt system at 467 K was measured to be 62.7 ± 3.9 nW/K extracted from a cantilever deflection of 0 nm (i.e., normal force of ~15 nN). The shaded regions show the 95% confidence interval of 13 measurements, while the solid line represents their average value.

shows the corresponding value of G_{expt}, which remains zero in the gap region, rapidly increases at snap in, and gradually increases as the cantilever is further pushed. The gradual increase of the thermal conductance is indicative of the onset of bulk contact and is attributed to the pressure dependence of the interfacial thermal resistance [22]. From this measurement, the BC thermal conductance (G_{BC}) between the Si tip and Pt nanoheater is determined to be 62.7 ± 3.9 nW/K at $z = 0$ nm. For proper comparison with the QTF-based experiments, the obtained G_{BC} is adjusted by considering the different effective contact areas. The adjusted thermal conductance, G_{BC}^*, is estimated to be 58.9 ± 3.7 nW/K and is shown in Figs. 4(a) and 6(a).

APPENDIX D: CALCULATION OF FORCE CONSTANTS FOR THE AGF METHOD

The short-range electron cloud interaction and van der Waals force are modeled via the L-J potential, while the long-range electrostatic surface charge interaction is modeled with the Coloumb force [74]. The L-J force constant is given by

$$k_{\mathrm{LJ}} = \left| 24\varepsilon \left[26 \left(\frac{\sigma^{12}}{\delta^{14}} \right) - 7 \left(\frac{\sigma^6}{\delta^8} \right) \right] \right|, \qquad \text{(D1)}$$

where $\varepsilon = 4.80 \times 10^{-20}$ J and $\sigma = 1.84 \times 10^{-10}$ m for the interaction between Pt and Si atoms (Pt-Si) [65]. The interatomic

force constant of Pt, $k_{\text{Pt}} = 6.31$ N/m, is obtained from Eq. (D1) using $\varepsilon = 1.09 \times 10^{-19}$ J and $\sigma = 2.54 \times 10^{-10}$ m for Pt-Pt interaction [65], whereas $k_{\text{Si}} = 6.16$ N/m is taken from Ref. [28] for Si-Si interaction. Although the tip used in the experiments is made of n-doped Si (phosphorus doped at 1×10^{18} cm^{-3}), it is treated as intrinsic Si in the AGF calculations because the elastic constant of n-doped Si is nearly the same as that of intrinsic Si for doping levels up to 8.5×10^{18} cm^{-3} [75].

The Coulomb force is mediated by surface charges. The Pt nanoheater sensing region has negative surface charges due to the applied bias voltage V_{bias} of 0.8 V as measured from the ground. By conceptualizing the Si tip as a floating ground, positive image charges are induced at the tip apex. Surface charges of opposite signs are the source of the Coulomb force. The Coulomb force constant due to surface charges is given by [76]

$$k_{\text{Coulomb}} = \left| \frac{Q_{\text{s}}}{4\pi\varepsilon_0} \left(\frac{2Q_s}{\delta^3} + \frac{3\varepsilon_0 V_{\text{bias}} A_{\text{tip}}}{\delta^4} \right) \frac{A_{\text{Si-Pt}}}{A_{\text{tip}}} \right|, \quad \text{(D2)}$$

where ε_0 is the permittivity of free space and Q_{s} is the surface charge ($= \sigma_{\text{s}} A_{\text{tip}}$, where σ_{s} is the surface charge density). Prediction of σ_{s} is challenging as it depends on the material properties, bias voltage, temperature, and gap distance. To constrain these parameters for our experimental condition, we extract σ_{s} from the gap-dependent Δf signal of the QTF at $d = 6$ nm, where Δf is independently measured from the nanoheater signals and contains the effects of those parameters onto the tip-sample force. It should be noted that the Coulomb force is expected to be dominant at $d = 6$ nm, which is in the NC regime.

At $d = 6$ nm, the lateral force is calculated to be 0.42 nN rms. In addition, we assume $\mu = 0.0005$ as the near-

contact friction coefficient that correlates the lateral force with the normal force. This value is within the acceptable range for the Si-Pt system with a nanoscale gap because experimental measurements of the contact μ value range from ~0.1 to ~0.01 depending on the contacting area [77]. Furthermore, molecular dynamics simulations for lubricated atomically flat surfaces in contact predicted $\mu \approx 0.001$ [78]. Using $\mu = 0.0005$, σ_{s} is estimated to be 8×10^{-4} C/m^2 using the Coulomb force equation [36]. We establish a confidence interval for the near-contact μ ranging from 0.001 to 0.0004, which corresponds to a surface charge density range of 6×10^{-4} to 1×10^{-3} C/m^2. These surface charge density values are in the reasonable range when compared with previous works [79–82] and used to determine the theoretical uncertainties in conjunction with the surface roughness distributions as shown in Figs. 6(a) and 6(b). It should be noted that at a small vacuum distance before contact, the Coulomb force vanishes due to charge neutralization [83]. The present work treats σ_{s} as a constant value that vanishes at a specific cutoff gap distance [84] due to the difficulty of describing its gap dependence. The cutoff distance is determined at the onset of electron tunneling across the vacuum gap, which is defined at an interatomic distance $\delta_c \approx 10$ Å [85,86].

APPENDIX E: INCORPORATION OF FORCE CONSTANTS INTO THE HARMONIC MATRIX

The force constants of the vacuum region due to the Lennard-Jones potential (k_{LJ}) and Coulomb interactions (k_{Coulomb}) are incorporated into the harmonic matrix H_{d} in Eq. (4) as follows [62]:

$$\boldsymbol{H}_{\text{d}} = \begin{bmatrix} \ddots & \vdots & \vdots & \vdots & \vdots & \cdot\cdot\cdot \\ \cdots & H_{\text{d}}^{4,4} & -k_{\text{Pt}}/m_{\text{Pt}} & 0 & 0 & \cdots \\ \cdots & -k_{\text{Pt}}/m_{\text{Pt}} & H_{\text{d}}^{5,5} & -(k_{\text{LJ}} + k_{\text{Coulomb}})/m_{\text{Si}} & 0 & \cdots \\ \cdots & 0 & -(k_{\text{LJ}} + k_{\text{Coulomb}})/m_{\text{Pt}} & H_{\text{d}}^{6,6} & -k_{\text{Si}}/m_{\text{Si}} & \cdots \\ \cdots & 0 & 0 & -k_{\text{Si}}/m_{\text{Si}} & H_{\text{d}}^{7,7} & \cdots \\ \cdot\cdot\cdot & \vdots & \vdots & \vdots & \vdots & \ddots \end{bmatrix}. \quad \text{(E1)}$$

The components of the harmonic matrix are described as $H_{\text{d}}^{j,k}$ ($j, k = 1, 2, \ldots, 10$). The force constants of the Pt and Si atoms are given by k_{Pt} and k_{Si} and their atomic weight is denoted as m_{Pt} and m_{Si}, respectively. The device region includes a total of 10 atoms (5 Si atoms for the left side and 5 Pt atoms for the right side), thus resulting in a 10×10 harmonic matrix. The diagonal components of H_{d} are calculated by

$$H_{\text{d}}^{j,j} = -\left(H_{\text{d}}^{j,j-1} + H_{\text{d}}^{j,j+1} \right). \quad \text{(E2)}$$

[1] A. Fiorino, D. Thompson, L. Zhu, R. Mittapally, S. A. Biehs, O. Bezencenet, N. El-Bondry, S. Bansropun, P. Ben-Abdallah, E. Meyhofer *et al.*, ACS Nano **12**, 5774 (2018).

[2] L. Zhu, A. Fiorino, D. Thompson, R. Mittapally, E. Meyhofer, and P. Reddy, Nature (London) **566**, 239 (2019).

[3] A. Fiorino, L. Zhu, D. Thompson, R. Mittapally, P. Reddy, and E. Meyhofer, Nat. Nanotechnol. **13**, 806 (2018).

[4] T. Inoue, T. Koyama, D. D. Kang, K. Ikeda, T. Asano, and S. Noda, Nano Lett. **19**, 3948 (2019).

[5] G. R. Bhatt, B. Zhao, S. Roberts, I. Datta, A. Mohanty, T. Lin, J. M. Hartmann, R. St-Gelais, S. Fan, and M. Lipson, Nat. Commun. **11**, 2545 (2020).

[6] C. Lucchesi, D. Cakiroglu, J.-P. Perez, T. Taliercio, E. Tournié, P.-O. Chapuis, and R. Vaillon, Nano Lett. **21**, 4524 (2021).

[7] E. Albisetti, D. Petti, M. Pancaldi, M. Madami, S. Tacchi, J. Curtis, W. P. King, A. Papp, G. Csaba, W. Porod *et al.*, Nat. Nanotechnol. **11**, 545 (2016).

[8] E. Rousseau, A. Siria, G. Jourdan, S. Volz, F. Comin, J. Chevrier, and J.-J. Greffet, Nat. Photon. **3**, 514 (2009).

[9] S. Shen, A. Narayanaswamy, and G. Chen, Nano Lett. **9**, 2909 (2009).

[10] B. Song, Y. Ganjeh, S. Sadat, D. Thompson, A. Fiorino, V. Fernández-Hurtado, J. Feist, F. J. Garcia-Vidal, J. C. Cuevas, P. Reddy *et al.*, Nat. Nanotechnol. **10**, 253 (2015).

[11] R. St-Gelais, L. Zhu, S. Fan, and M. Lipson, Nat. Nanotechnol. **11**, 515 (2016).

[12] M. P. Bernardi, D. Milovich, and M. Francoeur, Nat. Commun. **7**, 12900 (2016).

[13] B. Song, D. Thompson, A. Fiorino, Y. Ganjeh, P. Reddy, and E. Meyhofer, Nat. Nanotechnol. **11**, 509 (2016).

[14] J. I. Watjen, B. Zhao, and Z. M. Zhang, Appl. Phys. Lett. **109**, 203112 (2016).

[15] M. Ghashami, H. Geng, T. Kim, N. Iacopino, S. K. Cho, and K. Park, Phys. Rev. Lett. **120**, 175901 (2018).

[16] M. Lim, J. Song, S. S. Lee, and B. J. Lee, Nat. Commun. **9**, 4302 (2018).

[17] K. Kim, B. Song, V. Fernández-Hurtado, W. Lee, W. Jeong, L. Cui, D. Thompson, J. Feist, M. T. H. Reid, F. J. García-Vidal *et al.*, Nature (London) **528**, 387 (2015).

[18] J. DeSutter, L. Tang, and M. Francoeur, Nat. Nanotechnol. **14**, 751 (2019).

[19] L. Tang, J. Desutter, and M. Francoeur, ACS Photon. **7**, 1304 (2020).

[20] D. Polder and M. Van Hove, Phys. Rev. B **4**, 3303 (1971).

[21] S. Rytov, Y. Kravtsov, and V. Tatarskii, *Principles of Statistical Radiophysics* (Springer, New York, 1989), Vol. 3.

[22] B. Gotsmann and M. A. Lantz, Nat. Mater. **12**, 59 (2013).

[23] D. P. Sellan, E. S. Landry, K. Sasihithlu, A. Narayanaswamy, A. J. H. McGaughey, and C. H. Amon, Phys. Rev. B **85**, 024118 (2012).

[24] S. Xiong, K. Yang, Y. A. Kosevich, Y. Chalopin, R. D'Agosta, P. Cortona, and S. Volz, Phys. Rev. Lett. **112**, 114301 (2014).

[25] V. Chiloyan, J. Garg, K. Esfarjani, and G. Chen, Nat. Commun. **6**, 6755 (2015).

[26] A. Alkurdi, C. Adessi, F. Tabatabaei, S. Li, K. Termentzidis, and S. Merabia, Int. J. Heat Mass Transfer **158**, 119963 (2020).

[27] M. Prunnila and J. Meltaus, Phys. Rev. Lett. **105**, 125501 (2010).

[28] Y. Ezzahri and K. Joulain, Phys. Rev. B **90**, 115433 (2014).

[29] J. B. Pendry, K. Sasihithlu, and R. V. Craster, Phys. Rev. B **94**, 075414 (2016).

[30] J.-S. Wang and J. Peng, Europhys. Lett. **118**, 24001 (2017).

[31] K. Sasihithlu, J. B. Pendry, and R. V. Craster, Z. Naturforsch. A **72**, 181 (2017).

[32] Z.-Q. Zhang, J.-T. Lü, and J.-S. Wang, Phys. Rev. B **97**, 195450 (2018).

[33] P. S. Venkataram, J. Hermann, A. Tkatchenko, and A. W. Rodriguez, Phys. Rev. B **102**, 085403 (2020).

[34] A. I. Volokitin, J. Phys.: Condens. Matter **32**, 215001 (2020).

[35] W. Chen and G. Nagayama, Int. J. Heat Mass Transfer **176**, 121431 (2021).

[36] T. Tokunaga, A. Jarzembski, T. Shiga, K. Park, and M. Francoeur, Phys. Rev. B **104**, 125404 (2021).

[37] T. Tokunaga, M. Arai, K. Kobayashi, W. Hayami, S. Suehara, T. Shiga, K. Park, and M. Francoeur, Phys. Rev. B **105**, 045410 (2022).

[38] I. Altfeder, A. A. Voevodin, and A. K. Roy, Phys. Rev. Lett. **105**, 166101 (2010).

[39] A. Kittel, W. Muller-Hirsch, J. Parisi, S. A. Biehs, D. Reddig, and M. Holthaus, Phys. Rev. Lett. **95**, 224301 (2005).

[40] K. Kloppstech, N. Könne, S.-A. Biehs, A. W. Rodriguez, L. Worbes, D. Hellmann, and A. Kittel, Nat. Commun. **8**, 14475 (2017).

[41] L. Cui, W. Jeong, V. Fernández-Hurtado, J. Feist, F. J. García-Vidal, J. C. Cuevas, E. Meyhofer, and P. Reddy, Nat. Commun. **8**, 14479 (2017).

[42] See Supplemental Material at http://link.aps.org/supplemental/10.1103/PhysRevB.106.205418 for details concerning the experiments [43–46], verification of the 1D AGF method [23,26,47–51], and effect of bias voltage on tip-sample lateral force [28].

[43] D. Rugar, H. J. Mamin, and P. Guethner, Appl. Phys. Lett. **55**, 2588 (1989).

[44] S. Hamian, J. Yun, I. Park, and K. Park, Appl. Phys. Lett. **109**, 253114 (2016).

[45] K. Kim, W. Jeong, W. Lee, and P. Reddy, ACS Nano **6**, 4248 (2012).

[46] M. Asheghi, K. Kurabayashi, R. Kasnavi, and K. E. Goodson, J. Appl. Phys. **91**, 5079 (2002).

[47] N. Yu and A. A. Polycarpou, J. Colloid Interface Sci. **278**, 428 (2004).

[48] E. S. Landry and A. J. H. McGaughey, Phys. Rev. B **80**, 165304 (2009).

[49] S. Aubry, C. J. Kimmer, A. Skye, and P. K. Schelling, Phys. Rev. B **78**, 064112 (2008).

[50] W. Zhang, T. S. Fisher, and N. Mingo, J. Heat Transfer **129**, 483 (2007).

[51] D. P. Schroeder, Z. Aksamija, A. Rath, P. M. Voyles, M. G. Lagally, and M. A. Eriksson, Phys. Rev. Lett. **115**, 256101 (2015).

[52] K. Karrai and I. Tiemann, Phys. Rev. B **62**, 13174 (2000).

[53] A. Castellanos-Gomez, N. Agrait, and G. Rubio-Bollinger, Ultramicroscopy **111**, 186 (2011).

[54] R. D. Grober, J. Acimovic, J. Schuck, D. Hessman, P. J. Kindlemann, J. Hespanha, A. S. Morse, K. Karrai, I. Tiemann, and S. Manus, Rev. Sci. Instrum. **71**, 2776 (2000).

[55] P. J. Feibelman, B. Hammer, J. K. Nørskov, F. Wagner, M. Scheffler, R. Stumpf, R. Watwe, and J. Dumesic, J. Phys. Chem. B **105**, 4018 (2001).

[56] K. Esfarjani, G. Chen, and H. T. Stokes, Phys. Rev. B **84**, 085204 (2011).

[57] A. Jarzembski, S. Hamian, J. Yun, J. Crossley, I. Park, M. Francoeur, and K. Park, Rev. Sci. Instrum. **89**, 064902 (2018).

[58] J. P. Bentley, *Principles of Measurement Systems*, 3rd ed. (Longman Group Limited, Essex, England, 1995).

[59] S. Sadat, E. Meyhofer, and P. Reddy, Rev. Sci. Instrum. **83**, 084902 (2012).

[60] S. Edalatpour and M. Francoeur, Phys. Rev. B **94**, 045406 (2016).

[61] A. Jarzembski and K. Park, J. Quant. Spectrosc. Radiat. Transfer **191**, 67 (2017).

[62] S. Sadasivam, Y. Che, Z. Huang, L. Chen, S. Kumar, and T. S. Fisher, Annu. Rev. Heat Transfer **17**, 89 (2014).

[63] E. Clementi, D. L. Raimondi, and W. P. Reinhardt, J. Chem. Phys. **47**, 1300 (1967).

[64] J. Meija, T. B. Coplen, M. Berglund, W. A. Brand, P. De Bièvre, M. Gröning, N. E. Holden, J. Irrgeher, R. D. Loss, T. Walczyk *et al.*, Pure Appl. Chem. **88**, 265 (2016).

[65] E. B. Webb III and S. H. Garofalini, J. Chem. Phys. **105**, 792 (1996).

[66] A. B. Djurišić, J. M. Elazar, and A. D. Rakić, Appl. Opt. **36**, 7097 (1997).

[67] C. J. Fu and Z. M. Zhang, Int. J. Heat Mass Transfer **49**, 1703 (2006).

[68] S. Basu, B. J. Lee, and Z. M. Zhang, J. Heat Transfer **132**, 023301 (2010).

[69] T. Sun, K. Umemoto, Z. Wu, J.-C. Zheng, and R. M. Wentzcovitch, Phys. Rev. B **78**, 024304 (2008).

[70] Y. Mo, K. T. Turner, and I. Szlufarska, Nature (London) **457**, 1116 (2009).

[71] www.povray.org.

[72] C. W. Tsao, L. Hromada, J. Liu, P. Kumar, and D. L. DeVoe, Lab Chip **7**, 499 (2007).

[73] B. Derjaguin, V. Muller, and Y. Toporov, J. Colloid Interface Sci. **53**, 314 (1975).

[74] W. Shockley and G. L. Pearson, Phys. Rev. **74**, 232 (1948).

[75] N. Ono, K. Kitamura, K. Nakajima, and Y. Shimanuki, Jpn. J. Appl. Phys. **39**, 368 (2000).

[76] B. D. Terris, J. E. Stern, D. Rugar, and H. J. Mamin, Phys. Rev. Lett. **63**, 2669 (1989).

[77] B. Bhushan and K. J. Kwak, Nanotechnology **18**, 345504 (2007).

[78] J. Gao, W. D. Luedtke, D. Gourdon, M. Ruths, J. N. Israelachvili, and U. Landman, J. Phys. Chem. B **108**, 3410 (2004).

[79] Y. Yang, K. M. Mayer, and J. H. Hafner, Biophys. J. **92**, 1966 (2007).

[80] F. Johann and E. Soergel, Appl. Phys. Lett. **95**, 232906 (2009).

[81] D. El Khoury, R. Arinero, J. C. Laurentie, and J. Castellon, AIP Adv. **6**, 035318 (2016).

[82] L. H. Klausen, T. Fuhs, and M. Dong, Nat. Commun. **7**, 12447 (2016).

[83] S. H. Behrens and D. G. Grier, J. Chem. Phys. **115**, 6716 (2001).

[84] H.-J. Butt, Biophys. J. **60**, 777 (1991).

[85] D. Anselmetti, T. Richmond, A. Baratoff, G. Borer, M. Dreier, M. Bernasconi, and H. J. Güntherodt, Europhys. Lett. **25**, 297 (1994).

[86] L. S. McCarty and G. M. Whitesides, Angew. Chem. Int. Ed. **47**, 2188 (2008).